---

**Article:**
Murakami, S., Wang, D., Mostaed, A. orcid.org/0000-0002-2443-7819 et al. (6 more authors) (2018) High strain (0.4%) Bi(Mg2/3Nb1/3)O3-BaTiO3-BiFeO3 lead-free piezoelectric ceramics and multilayers. Journal of the American Ceramic Society, 101 (12). pp. 5428-5442. ISSN 0002-7820

https://doi.org/10.1111/jace.15749

---

# High strain (0.4%) $Bi(Mg_{2/3}Nb_{1/3})O_3$-$BaTiO_3$-$BiFeO_3$ lead-free piezoelectric ceramics and multilayers

Shunsuke Murakami[1], Dawei Wang[1], Ali Mostaed[1], Amir Khesro[1], Antonio Feteira[2], Derek C. Sinclair[1], Zhongming Fan[3], Xiaoli Tan[3] and Ian M Reaney[1, *]

[1]Department of Materials Science and Engineering, University of Sheffield, Sheffield S1 3JD, UK

[2]Materials Engineering and Research Institute, Sheffield Hallam University, Sheffield S1 1WB, UK

[3]Department of Materials Science and Engineering, Iowa State University, Ames, Iowa, 50011 USA

*Corresponding Author Prof. Ian M Reaney: i.m.reaney@sheffield.ac.uk

## Abstract

The relationship between the piezoelectric properties and the structure/microstructure for $0.05Bi(Mg_{2/3}Nb_{1/3})O_3$-$(0.95-x)BaTiO_3$-$xBiFeO_3$ (BBFT, x = 0.55, 0.60, 0.63, 0.65, 0.70, and 0.75) ceramics has been investigated. Scanning electron microscopy revealed a homogeneous microstructure for $x < 0.75$ but there was evidence of a core-shell cation distribution for x = 0.75 which could be suppressed in part through quenching from the sintering temperature. X-ray diffraction (XRD) suggested a gradual structural transition from pseudocubic to rhombohedral for $0.63<x<0.70$, characterised by the coexistence of phases. The temperature dependence of relative permittivity, polarisation-electric field hysteresis loops, bipolar strain-electric field curves revealed that BBFT transformed from relaxor-like to ferroelectric behaviour with an increase in x, consistent with changes in the phase assemblage and domain structure. The largest strain was 0.41 % for x = 0.63 at

10kV/mm. The largest effective piezoelectric coefficient ($d_{33}^*$) was 544 pm/V for $x = 0.63$ at 5 kV/mm but the largest Berlincourt $d_{33}$ (148 pC/N) was obtained for x = 0.70. We propose that $d_{33}^*$ is optimised at the point of crossover from relaxor to ferroelectric which facilitates a macroscopic field induced transition to a ferroelectric state but that $d_{33}$ is optimised in the ferroelectric, rhombohedral phase. Unipolar strain was measured as a function of temperature for $x = 0.63$ with strains of 0.30% achieved at 175ºC, accompanied by a significant decrease in hysteresis with respect to room temperature measurements. The potential for BBFT compositions to be used as high strain actuators is demonstrated by the fabrication of a prototype multilayer which achieved 3 μm displacement at 150 ºC.

## 1. Introduction

Piezoelectric materials convert electrical energy to mechanical strain and vice versa and have applications, such as actuators, sensors, generators and acoustic transducers. Recently, piezoelectric applications have emerged for extreme environment such as within the high temperature (>200 ºC) regions of automotive engines. Consequently, there has been significant interest to improve the temperature range and performance of piezoelectrics and an acceptance that compositions with higher Curie temperature ($T_C$)

than $Pb(Zr,Ti)O_3$ (PZT) (250-320 ºC) are required to achieve this ambition[1, 2]

PZT has been widely applied in piezoelectric devices over the past few decades.[3] However, not only are there limitations in its operating temperature,[1,2] but there are also environment and health issues due to the toxicity of lead.[4,5] Rödel *et al.* [6] summarized how lead affects the human body, noting that PbO is less toxic than metallic Pb. The majority of potential problems for PZT are linked not to the stable room temperature compound but during production when lead oxide is vaporized at high temperature.[7-9] Potential EU legislation banning PbO in the manufacture of piezoelectrics has therefore led to the development of a range of lead-free materials based on $(K,Na)NbO_3$ (KNN), $Na_{1/2}Bi_{1/2}TiO_3$ (NBT), and $(Ba,Ca)(Zr,Ti)O_3$ (BCZT). Each PbO-free alternative has strong and weak points. KNN based materials nominally have a high $T_C$ and high piezoelectric coefficient ($d_{33}$ > 300)[10] but they generally exhibit a decrease in piezoactivity with increase in temperature.[11,12] However, we note that Wang et al.[13, 14] reported the composition, $0.92(Na_{0.5}K_{0.5})NbO_3$-$0.06(Bi_{1/2}Li_{1/2})TiO_3$-$0.02BaZrO_3$, to have 348 pC/N at RT which only decreased to around 200 pC/N at 200 ºC.

NBT based materials need a high driving electric field to achieve large strain and undergo depolarization at relatively low temperatures (~150 ºC). High strain compositions (>0.35%) are also highly hysteretic.[15] BCTZ based materials show high

piezoelectric performance at the expense of a low $T_C$ (<100 ºC).[16, 17]

$BaTiO_3$-$BiFeO_3$ (BT-BF) based ceramics have been reported to have high piezoelectric coefficient $d_{33}$ = 402 pC/N and high $T_C$ = 454ºC after quenching.[18] However, there are real challenges in convincing industry that quenched BT-BF ceramics and multilayers are mechanically reliable. Nonetheless, BT-BF compositions offer an important starting point for the development of piezoelectric materials which potentially have high strain (>0.3%) with $T_C$ higher than PZT (>300 ºC).

PZT is known to have an optimised $d_{33}$ and electromechanical coupling coefficient ($k$) at a morphotropic phase boundary (MPB).[19,20] BT-BF ceramics are also considered to exhibit an MPB.[21-25] Wei et al. [22] reported that 0.30BT-0.70BF (MPB composition) shows the highest $d_{33}$ of 134 pC/N whereas Kumar and co-workers[25] suggested that (1-$x$)BT-$x$BF ceramics transform from tetragonal to rhombohedral at $0.5<x<0.6$, at which compositions the structure appears to be pseudocubic. In general, there is no clear consensus concerning the changes in crystal structure as a function of composition within the BT-BF system,[20-26] suggesting that multiple factors such as sintering conditions, quenching and dopants affect the phase assemblage. The same is true of microstructure. Yabuta et al.[27] reported about the compositional inhomogeneity of (1-$x$)(0.33$BaTiO_3$-0.67$BiFeO_3$)-$x$Bi($Mg_{1/2}Ti_{1/2}$)$O_3$ ($x$ = 0, 0.05, 0.10, and 0.15) ceramics but there have been

few papers referring to the relationships between the microstructure and the properties in the systematic investigation of BT-BF. Further work is thus required to design the composition and dopants of the BT-BF system to understand and optimise structure-property relations.

Many researchers (e.g. refs 25, 26) have suggested that the leakage current in $BiFeO_3$ containing systems originates from either the loss of Bi or from the formation of $Fe^{2+}$ as opposed to $Fe^{3+}$ during sintering. They have also proposed that various dopants alleviate these problems.[28, 29] Dopants in the field of piezoelectric materials are classified into three groups; donor (higher valence), acceptor (lower valence) and self-compensated (average valence number remains the same). All the above-mentioned dopant strategies improve the resistivity of BT-BF ceramics as reported in the literature.[11, 19, 20, 30-42] Wang et al. [30] reported that Nb (donor) improves the resistivity of BT-BF while it gives rise to a decrease in the grain size. Curiously, acceptor dopants also improve the resistivity of BT-BF.[33, 34] For instance, as Yao and co-workers[33] reported, Mn increases the resistivity and decreases the dielectric loss of 0.8BF-0.2BT ceramics. However, the most successful dopants are stoichiometric or self-compensated (e.g. Cr, Co, Al, Ga, $Mg_{1/2}Ti_{1/2}$, $Zn_{1/2}Ti_{1/2}$ and $Ni_{1/2}Ti_{1/2}$) which improve not only the resistivity of furnace cooled ceramics but also their piezoelectric properties.[18, 35-42] Nonetheless, the $d_{33}$ of furnace-cooled doped BF-BT

compositions is typically much smaller (163 pC/N) than that of quenched samples.[16, 39]

Given that all dopant strategies appear empirically to improve resistivity and stoichiometric/self-compensated dopants improve $d_{33}$, it is logical to design doped compositions which not only act locally as aliovalent dopants but which also maintain macroscopic stoichiometry. The base composition has a mixture of $Fe^{3+}$ and $Ti^{4+}$ on the B-site. Consequently, only 2+ ions (e.g. $Mg^{2+}$) will consistently act as an acceptor irrespective of where they substitute in the lattice. A similar argument can be made for donor 5+ species (e.g. $Nb^{5+}$) which will act as a local donor wherever they substitute on the B-site. Substituting in the ratio $Mg_{2/3}Nb_{1/3}$ maintains macroscopic stoichiometry (assuming an average 3+ valence) by creating a self-compensated combined dopant and follows previous work on stoichiometric dopants, e.g. $Bi(Mg_{1/2}Ti_{1/2})O_3$-$BaTiO_3$-$BiFeO_3$, reported by other researchers.[27, 29] However, the higher valence of $Nb^{5+}$ in comparison to $Ti^{4+}$ ensures the universal presence of a donor as well as acceptor ion ($Mg^{2+}$). To ensure that all grains contain both acceptor and donor ions, 5 mol% of $Bi(Mg_{2/3}Nb_{1/3})O_3$ was substituted into the $BaTiO_3$ – $BiFeO_3$ solid solution in accordance with the formula, $0.05Bi(Mg_{2/3}Nb_{1/3})O_3$-$(0.95-x)BaTiO_3$-$xBiFeO_3$ in which x was systematically varied to optimise properties.

## 2. Experimental procedure

$0.05Bi(Mg_{2/3}Nb_{1/3})O_3$-$(0.95-x)BaTiO_3$-$xBiFeO_3$ (x = 0.55, 0.60, 0.63, 0.65, 0.70, and 0.75) ceramics were prepared by conventional solid-state methods. The starting raw materials were as follows; $Bi_2O_3$ (99.9%, Acros Organics), $Fe_2O_3$ (99%, Sigma Aldrich), $BaCO_3$ (99%, Sigma Aldrich), $TiO_2$ (99.9%, Sigma Aldrich), MgO (99%, Sigma Aldrich), and $Nb_2O_5$ (99.5%, Alfa Aesar). The raw materials were dried overnight to eliminate moisture, hydroxide, and adsorbed $CO_2$ before weighing. The dried powders were weighed and attrition milled for 1 to 2 h at 300 rpm in a Union Processes attritor mill (Szegvari Attritor System, Union Process), using 3mm diameter yttria-stabilised zirconia media in isopropanol. The slurry was separated from the media and dried overnight at 80ºC. The mixed dried powder was calcined at 750 to 800ºC in an $Al_2O_3$ crucible for 2 h in a muffle furnace. The calcined powder was further attrition milled and dried. The attrition milled powder was mixed with poly(vinyl alcohol) equal to 0.5wt% of the attrition milled powder, dried, pulverized by using an agate pestle and mortar, and sieved through 250 micron mesh. ~ 0.3 g of powder was uniaxially pressed into a disk with 10 mm diameter at 125 MPa to form a compact. The compacts were sintered between 960 to 1040ºC for 2h after burning out the binder at 550ºC. To evaluate the electric, dielectric, and piezoelectric properties, silver paste electrodes were applied to the sintered pellets,

and then heated at 500ºC for 2 h.

To measure X-ray powder diffraction (XRD), the sintered pellets were crushed and ground to fine powder. XRD was performed using a Bruker D2 phaser X-ray diffractometer with CuKα (Bruker). The microstructure of polished/thermally etched pellets were studied using a scanning electron microscope (SEM) equipped with a backscattered electron detector (BSE) (Phillips, XL30). The surfaces of the samples were ground and mirror polished using wet abrasive paper. Samples were further polished using diamond abrasives in a water-based Diamond lubricant (MetPrep Ltd.). The polished samples were thermally etched at 900ºC for 20 minutes. Transmission electron microscopy (TEM) samples were prepared by grinding and polishing the ceramic to <30 μm followed by ion beam milling by a GATAN precision ion polishing (PIPS) II (GATAN) to electron transparency. Some samples were mechanically dimpled to 10 μm prior to ion milling. Samples were examined using a either JEOL R005 TEM (JEOL) operating at 300 kV or a Tecnai G2-F20 transmission electron microscopy operating at 200 kV. All crystallographic diffraction notation relates to a pseuducubic fundamental perovskite cell.

$\varepsilon_r$ and tan$\delta$ were measured at 10 kHz using a LCR meter (HP, 4284A). The temperature dependence of the $\varepsilon_r$ and tan$\delta$ were measured from 20 to 700ºC. Polarisation-

Electric field (PE) hysteresis loops were measured at 1 Hz in silicone oil at room temperature in a ferroelectric tester (AixACCT, TF 2000). The impedance was measured from 100 to 500ºC in the frequency range 5 Hz to 13 MHz using a Precision LCR Meter (Agilent, E4980A). $d_{33}$ was measured with a piezoelectric meter (PiezoMeter System, PIEZOTEST) shortly after poling. The poling treatment was conducted in silicone oil at 90 to 100ºC under DC at 40 to 50 kV/cm for 20 minutes. Electric field-induced strain (SE) was measured at 1 Hz up to 10 kV/cm from room temperature to 175ºC in silicone oil using a ferroelectric tester (AixACCT, TF 2000).

For multilayer actuators (MLA), calcined and attrition milled powder was mixed with ethyl methyl ketone (Fisher Chemical) as a solvent, poly(propylene carbonate) (EMPOWER Materials) as both dispersant and binder, and butyl benzyl phthalate (Sigma-Aldrich) as a plasticizer using Speed-mixer DAC 800 FVZ (Hauschild Engineering). The slurry was cast onto a silicon coated polyethylene terephthalate (PET) carrier film using a Mistler TCC-1200 tapecaster with a single doctor blade. The cast slurry was dried 1 h at room temperature. Pt ink (M637C Heraeus Electronic Materials) was printed on the green ceramics tapes using a DEK 247 screen printer. The size of each internal electrode area was 9.2 mm × 7.2 mm. 6 green ceramics tapes with Pt internal electrodes were laminated and pressed at 10 MPa at 70ºC for 20 min. The pressed green sheets were

sintered at 1005ºC for 2h after burning out organic ingredients at 180 and 300ºC.

## 3. Results and discussion

### 3.1 XRD Analysis

XRD diffractograms of $0.05Bi(Mg_{2/3}Nb_{1/3})O_3$-$(0.95-x)BaTiO_3$-$xBiFeO_3$ (x = 0.55, 0.60, 0.63, 0.65, 0.70, and 0.75) ceramics are shown in Figure1. All patterns indexed according to a perovskite structure with no secondary phase peaks present. In addition, to determine the most probable structure for each data set, Rietveld refinements were conducted (Table 1). As *x* increased from 0.55 to 0.75, a systematic change in structure occurred from pseudocubic (*Pm-3m*) to mixed pseudocubic (*Pm-3m*) and rhombohedral (*R3c*) with the ratio of *R3c/Pm-3m* generally increasing with *x* as the $BiFeO_3$ end member is approached. The Miller indices in the XRD traces of x = 0.55 and x =0.75 in Figure 1 are in the pseudocubic (*Pm-3m*) and rhombohedral (*R3c*) settings, respectively.

### 3.2 Microstructure

To investigate the microstructure and the compositional homogeneity of ceramics, BSE images for the $0.05Bi(Mg_{2/3}Nb_{1/3})O_3$-$(0.95-x)BaTiO_3$-$xBiFeO_3$ ceramics were acquired (Figure 2). For all samples except x =0.75, most grains were in the range of 5 to

10 µm and image contrast suggested a homogeneous composition, indicating $Mg^{2+}$ (0.72 Å) nm and $Nb^{5+}$ (0.64 Å) reside on the B site (Fe, 0.645 Å and Ti, 0.601 Å). However, for x = 0.75, grains were < 5 µm, smaller than in other samples with evidence of a core-shell structure with darker and brighter contrast, relating to regions of lower ($BaTiO_3$-rich) and higher ($BiFeO_3$-rich) weight average atomic number consistent with energy dispersive X-ray analysis (not shown here).

Figure 3 (a) is a dark field two beam TEM image of a sample with x = 0.63 obtained using a 111 reflection with the electron beam approximately parallel to a [110] direction. There is no evidence of long range polar order (no distinct domain walls) and only local correlation of fringe contrast, typical of a pseudocubic (XRD data in Figure 1), relaxor-like compound with a nano- rather than macro- domain structure. Inset in Figure 3 (a) is a [110] zone axis diffraction pattern. Only fundamental perovskite spots appear in the pattern with no superstructure reflections, indicating the absence of octahedral tilting. In contrast, Figure 3 (b) shows a bright field image near a [112] direction for samples with x = 0.7 which shows an R3c phase, consistent with the XRD data, Figure 1. The R3c phase is characterised by lamellar ferroelectric domains with corresponding diffraction patterns exhibiting ½{ooo} antiphase tilting superstructure reflections in some but not all <112> zone axes. Two variants of the <112> zone axes (with and without ½{ooo}) are included

in Figure 3b. Please note that on tilting the sample lamellar domains may also be observed in the upper RHS of the image.

To evaluate the electrical homogeneity, impedance spectroscopy (IS) analysis was conducted. Spectroscopic plots of *Z"* and *M"* extracted from impedance spectroscopy data may be used as a simple means to qualitatively assess electrical homogeneity. Figure 4 (a-f) show *Z"* and *M"* from complex *IS* plots with frequency for the $0.05Bi(Mg_{2/3}Nb_{1/3})O_3$-(0.95-x)$BaTiO_3$-x$BiFeO_3$ ceramics. For $x$ = 0.55 to 0.70, the measurements were conducted at 320ºC. For $x$ = 0.75, the measurement was conducted at 180ºC to ascertain the entire shape of the spectrum of *Z"* and *M"*. All the spectra of *M"* show a main peak and the low frequency tail of a second, higher frequency peak, indicating that they all have two or more electrical phases, most likely relating to either grain boundary, shell or core regions. The capacitance calculated from $Z''_{max}$ measured at 320ºC for the $0.05Bi(Mg_{2/3}Nb_{1/3})O_3$-(0.95-x)$BaTiO_3$-x$BiFeO_3$ ceramics are shown in Table 2. For $x$ = 0.55 to 0.65, the capacitance values are ~ 1 to 2 nF which is consistent with a grain boundary type-response but the capacitance decreases to 0.43 nF for $x$ = 0.70 and 0.13 nF for $x$ = 0.75 and these lower values are more indicative of a shell-type response. For $x$ = 0.75 there is a clear gap between the peak positions of *Z"* and *M"*, indicating the main electric path is electrically heterogeneous which may correspond to

compositional inhomogeneity shown in the BSE image.

The total electrical conductivity ($\sigma_{dc} = 1/R$) was calculated from the low frequency intercept of the large arc in the $Z^*$ plots which corresponds to the large $Z''$ peak observed in Figure 4 (a-f), $\sigma_{dc}$ versus reciprocal temperature for the $0.05Bi(Mg_{2/3}Nb_{1/3})O_3$-$(0.95-x)BaTiO_3$-$xBiFeO_3$ ceramics are shown in Figure 5 and the activation energy ($E_a$) calculated from these plots are shown in Table 2. Figure 4. shows that $x = 0.75$ is more conductive than the others. For $x = 0.75$, the $E_a$ is clearly smaller, which means there is an obvious difference in the conduction mechanism between $x$ =0.55 to 0.65 and $x = 0.75$ and supports the conductivity results. Furthermore, these data imply that the electric path which show high resistivity for $x = 0.55$ to 0.65 is not present in $x = 0.75$. In other words, when compositions are microstructurally homogeneous (e.g. x = 0.55 to 0.65) a high resistive electric path is maintained. The high resistive electrical path is tentatively attributed to a grain boundary response but further measurements are required to confirm this assignment.

### 3.3 Temperature dependence of relative permittivity ($\varepsilon_r$) and tanδ

The temperature dependencies of $\varepsilon_r$ and $\tan\delta$ for the $0.05Bi(Mg_{2/3}Nb_{1/3})O_3$-$(0.95-x)BaTiO_3$-$xBiFeO_3$ ceramics are shown in Figure 6(a) and 6(b) (measured at 10 kHz). For

$x$ = 0.55 (Figure 6(a)), the diffuse dielectric anomaly is broadly consistent with a relaxor-like transition and concomitant with the pseudocubic structure refined from XRD data. As $x$ increases to $x$ = 0.70, the dielectric anomalies sharpen as the volume fraction of the ferroelectric (*R3c*) phase in structural refinements increases. However, for $x$ = 0.75, a broad flat diffuse dielectric anomaly is observed suggesting that this composition is no longer homogeneous, as confirmed by BSE images and *Z"*, *M"* impedance plots.

The frequency dependence of $\varepsilon_r$ and tan$\delta$ vs temperature for $0.05Bi(Mg_{2/3}Nb_{1/3})O_3$-$(1-x)BaTiO_3$-$xBiFeO_3$ ceramics ($x$ = (a) 0.55, (b) 0.63, (c) 0.70) measured at 1, 10, 100, and 250kHz are shown in Figure 7. For $x$ = 0.55, the dielectric anomaly and tan$\delta$ shift to high temperature as the frequency increases, indicating these ceramics are relaxors. For $x$ = 0.70, the diffuse dielectric anomaly also shifts in a similar manner to $x$ = 0.55 but by a smaller interval, probably due to the difference of the ratio of relaxor-like to ferroelectric-like phase. However, for $x$ = 0.63, the diffuse dielectric anomaly decreased but did not shift from 10 kHz to 100 kHz. The reason for the absence of classic relaxor-like behaviour is not clear but may relate to the presence of multiple phase transitions which obscure the trends expected for pseudocubic ceramics which contain short range ordered polar nanoregions, as evidenced by XRD (Figure 1) and TEM (Figure 3).

Tan$\delta$ for all compositions at room temperature is typically <0.1 and for $0.55 \leq x \leq 0.65$ does not increase significantly until >350°C which is encouraging for high temperature applications. However, for $x \geq 0.70$ the onset of the sharp increase in dielectric loss shifts to lower temperatures, consistent with a chemically and electrically inhomogeneous microstructure observed by BSE images and *Z"*, *M"*, impedance plots, respectively.

### 3.4 Ferroelectric and Piezoelectric properties

*PE* hysteresis loops and bipolar *SE* curves for the $0.05Bi(Mg_{2/3}Nb_{1/3})O_3$-$(0.95-x)BaTiO_3$-$xBiFeO_3$ ceramics were measured under an electric field of 7 kV/mm at room temperature (Figure 8(a) and Figure 8(b)). *PE* hysteresis loops show a change from a narrow hysteresis loop, more typical of electrostrictive compositions with limited or no long-range ferroelectricity to a classic ferroelectric square loop as $x$ increases until 0.7, consistent with the increase in volume fraction of the *R3c* phase. A similar trend is observed for bipolar strain field measurements which transform from loops commensurate with dominant electrostrictive behaviour (negligible negative strain) to classic butterfly loops typical of a long-range order ferroelectric. However, $x = 0.75$ does not exhibit ferroelectric hysteresis and shows negligible strain, concomitant with an electrically and chemically inhomogeneous ceramic. Unpoled samples with $x = 0.63$

recorded the maximum strain of 0.41% at 10kV/mm at room temperature (Figure 9 (a)). We note however, that the largest $d_{33}^*$ was obtained for this composition in the poled state, notably at 5kV/mm rather than 10 kV/mm (544 pm/V), Figure 9 (b). We further note that the largest strains/$d_{33}^*$ are recorded at the point of crossover from dominant relaxor, electrostrictive ($x$<0.63) to ferroelectric behaviour (0.65≤$x$≤0.70), a trend previously observed in Pb-free systems based on NBT or $(K_{0.5}Bi_{0.5})TiO_3$ (KBT).[43-45]

The temperature dependence of the unipolar *SE* curves for poled $0.05Bi(Mg_{2/3}Nb_{1/3})O_3$-(0.95-x)$BaTiO_3$-x$BiFeO_3$ (x = 0.63) ceramics measured under an electric field of 6 kV/mm from 25 to 175ºC are shown in Figure10. The strain increased from ~0.27 to ~0.34% at 100 ºC and decreased to ~0.30% at 175 ºC accompanied by a notable decrease in hysteresis with respect to room temperature measurements. The variation of strain ($\Delta S$) was 25%. Comparison of the variation with PZT and other PbO free materials is given in table 3. These results suggest that BBTF may have the potential to operate at higher temperatures than typical for PbO-free ceramics which often have low depolarising temperatures or a decrease in piezoactivity as temperature increases. [45-49]

Figure 11 compares $d_{33}^*$ calculated from unipolar strain and $d_{33}$ for poled $0.05Bi(Mg_{2/3}Nb_{1/3})O_3$-(0.95-x)$BaTiO_3$-x$BiFeO_3$ (x = 0.55, 0.60, 0.63, 0.65, 0.70, and

0.75) ceramics. The largest $d_{33}$ was 148 pC/N for $x = 0.70$ and the largest $d_{33}^*$ was 544 pm/V for $x = 0.63$ at 5 kV/mm. We note that the maximum $d_{33}$ and $d_{33}^*$ are not coincident, suggesting that the large strains relate principally to a field induced transition to a ferroelectric state rather than classic extender piezoelectric behaviour.[50-55] A conclusion supported but the absence of evidence of long range polar order in the TEM images (Figure 3) and the pseudocubic structure in XRD data (Figure 1) for high strain compositions.

### 3.5 **Effect of quenching on $0.05Bi(Mg_{2/3}Nb_{1/3})O_3$-$0.75BaTiO_3$-$0.20BiFeO_3$**

To investigate the cause of the compositional inhomogeneity for $0.05Bi(Mg_{2/3}Nb_{1/3})O_3$-$(0.95-x)BaTiO_3$-$xBiFeO_3$ (x = 0.75), quenched (into liquid $N_2$) were compared to furnace cooled samples. Figure 12 (a) and (b) show BSE images for polished $0.05Bi(Mg_{2/3}Nb_{1/3})O_3$-$(0.95-x)BaTiO_3$-$(x)BiFeO_3$ (x = 0.75) of furnace cooled and quenched samples. For the furnace cooled composition, the core shell structure is apparent in the BSE images but less evident in the quenched sample under identical imaging conditions. Moreover, ferroelectric macrodomains are observed in the quenched but not in the furnace cooled sample, consistent with the PE and SE loops, Figure 13 (a) and (b). We note however, that there is a bright presumably Bi rich phase in the grain

boundary of the quenched sample. This might suggest a complex phase equilibrium at the sintering temperature, involving a Bi-rich grain boundary phase in addition to the perovskite matrix phase. It is nonetheless concluded that the inhomogeneous distribution of constituent ions in the matrix phase was generated during furnace cooling.

*PE* hysteresis loops and bipolar *SE* curves for furnace cooled and quenched samples measured at room temperature at 8 kV/mm are shown in Figure 13 (a) and (b). The *PE* hysteresis loop of the furnace cooled sample is elliptical which indicates that the ceramics have only a weak ferroelectric response but quenched samples show square hysteresis loops typical of a ferroelectric. Moreover, the furnace cooled sample reveals negligible strain in bipolar measurements but the *SE* curve of the quenched sample shows a butterfly-like shape consistent with a strong ferroelectric/piezoelectric response. We conclude therefore, that improved homogeneity in the matrix phase for quenched samples results in superior piezoelectric and ferroelectric properties in $0.05Bi(Mg_{2/3}Nb_{1/3})O_3$-$(0.95-x)BaTiO_3$-$xBiFeO_3$ (x = 0.75) ceramics. The onset of inhomogeneity in the matrix suggests that x = 0.75 cools from a single perovskite phase at the sintering temperature through to a lower temperature region in which two perovskite phases co-exist.

We note that the largest strains in the BBFT system occur at x = 0.63 at the relaxor-ferroelectric crossover, a composition which remains homogeneous during furnace

cooling, i.e. has a single perovskite phase over the entire temperature range from sintering. We speculate that not only is the $Mg_{2/3}Nb_{1/3}$, self-compensated dopant important in controlling conductivity in these systems, but it also encourages the formation of a relaxor-ferroelectric point of crossover (high strain/$d_{33}^*$) in compositions which are intrinsically homogenous (miscible over large temperature ranges), effectively moving the perovskite immiscibility region away from the 'sweet-spot' for high strain and large $d_{33}^*$, thereby removing the need for quenching, alluded to by several authors.[18,39]

### 3.6 Multilayer actuator for $0.05Bi(Mg_{2/3}Nb_{1/3})O_3$-$0.63BaTiO_3$-$0.32BiFeO_3$

To demonstrate the potential of BBFT compositions for commercialisation, a MLA of $0.05Bi(Mg_{2/3}Nb_{1/3})O_3$-$0.63BaTiO_3$-$0.32BiFeO_3$ was fabricated. Figure 14 (a) is a scanning electron microscope image (SEM) of a cross section of a MLA. The thickness of each ceramic layer was ~120 μm and the active area of each electrode was 34.34 $mm^2$. No delamination or voids were observed. PE hysteresis loop and bipolar SE curve for a MLA measured at room temperature are shown in Figure 14 (b). The MLA gave a displacement of ~1.5 μm at 882V (7 kV/mm) with a similar strain (0.25%) to bulk compositions. The maximum polarization was 38 μC/$cm^2$, slightly smaller than that of the bulk ceramics, (41 μC/$cm^2$). The SE and PE hysteresis loops are however a little wider

in MLAs than in bulk ceramics, perhaps suggesting some influence of clamping on domain wall motion from the presence of the internal Pt electrode. Figure 14 (c) and (d) show the temperature dependence of unipolar SE curve and PE loop for the MLA measured under an electric field of 6 kV/mm from 25 to 150ºC. The strain increases from a displacement of 1.5 μm to >3 μm from room temperature to 150 ºC. Although strain increases in bulk ceramics with increase in temperature, the magnitude is significantly less (only 20% increase in bulk). The origin of this difference in the temperature dependence of strain between bulk and MLA remains to be elucidated but is likely to relate to un-pinning/clamping of domain walls as temperature increases.

These novel compositions based on BBFT represent an important set of materials in the search for lead free electrostrictors and piezoelectrics. Although their small signal $d_{33}$ is unsuitable for sensor applications, their large electrostrictive response and high strain (0.4%) are competitive with, or superior to, many lead free piezoelectrics for actuator applications.[6] The inclusion of $Mg_{1/3}Nb_{2/3}$ as stoichiometric co-dopants was initially performed to modify the defect chemistry and reduce conductivity but it is evident from the results presented that $Mg^{2+}$ and $Nb^{5+}$ on the B-site also affect the correlation length of dipolar coupling and encourage the onset of relaxor rather than ferroelectric behaviour, thus permitting the large dominantly, electrostrictive strains.

BBFT is composed of non-toxic and environmentally sustainable elements with the exception of $Nb_2O_5$ but the low wt% in BBFT (<2 wt%) in comparison to KNN (60 wt%) ensures that its environmental profile is superior.[56] Compared to NBT, KNN and BCZT there are relatively few studies of BBFT based compositions but the large strains and multilayer fabrication for non-quenched compositions demonstrated in our study suggest they are worthy of further investigation.

## 4. Conclusions

The relationship between the piezoelectric/electrostrictive properties, the structure and microstructure for $0.05(Mg_{2/3}Nb_{1/3})O_3$-$(0.95-x)BaTiO_3$-$xBiFeO_3$ (x = 0.55, 0.60, 0.63, 0.65, 0.70, and 0.75) ceramics was investigated. XRD revealed that compositions gradually transformed from a pseudocubic (Pm-3m) to a rhombohedral (R3c) phase as x increased. BSE images and *Z"*, *M"* spectroscopic plots showed that x = 0.75 is chemically heterogeneous and has the greatest electrical inhomogeneity. The temperature dependence of the relative permittivity showed Curie maxima, consistent with a crossover from relaxor-like to ferroelectric behaviour as x increased with TEM images and polarisation - strain - field behaviour also coherent with this premise. The largest $d_{33}^*$ was measured at 544 pm/V for $x$ = 0.63 under 5 kV/mm at the crossover from relaxor to

ferroelectric behaviour. The temperature dependence for $x$ = 0.63 showed 0.30% strain under an electric field of 6 kV/mm at 175 ºC with a notable decrease in hysteresis with respect to room temperature. For $x$ = 0.75, quenching improved the chemical homogeneity in the perovskite phase and resulted in significantly improved ferroelectric and piezoelectric properties. We propose that not only is the $Mg_{2/3}Nb_{1/3}$, self-compensated dopant important in controlling conductivity in BT-BF based systems, but also encourages a relaxor-ferroelectric point of cross over in compositions which are miscible over large temperature ranges, effectively moving the immiscibility region away from the 'sweet-spot' for high strain and large $d_{33}^*$, thereby removing the need for quenching. BBFT composition were successfully fabricated into MLAs with properties similar to bulk but with a marked increase in the temperature dependence of strain.

**Acknowledgements**

We thank the EPSRC for funding (Substitution and Sustainability in Functional Materials and Devices, EP/L017563/1).

**References**

1 T. Stevenson, D. G. Martin, P. I. Cowin, A. Blumfield, A. J. Bell, T. P. Comyn, and P. M. Weaver, Piezoelectric materials for high temperature transducers and actuators, *J. Mater. Sci. Mater. Electron*, **26**, 9256-9267 (2015).

2 R. Müller-Fielder and V. Knoblauch, Reliability aspects of microsensors and micromechatronic actuators for automotive applications, *Microelectron. Reliab*,

**43**, 1085-1097 (2003).

3 *An Introduction to Piezoelectric Materials and Applications*, J. Holterman & P. Groen.

4 R. A. Goyer, Lead Toxicity: Current concerns, *Environ Health Perspect*, **100**, 177-187 (1993).

5 G. Lockitch, Perspectives on Lead Toxicity, *Clin Biochem,***26**, 371-381 (1993).

6 J. Rödel, K G. Webber, R. Dittmer, W. Jo, M. Kimura, and D. Damjanovic, Transferring lead-free piezoelectric ceramics into application, *J Eur Ceram Soc*, **35**, 1659-1681 (2015).

7 A. Takahashi, Problems of gum and plastic products from the point of food hygiene, *Nippon Gomu Kyokaishi*, **48**, 537-557 (1975).

8 Canadian Centre for Occupational Health and Safety. *Material and safetydata sheet on lead oxide*, (1995).

9 K.H. Härdtl, H. Rau, PbO vapour pressure in the $Pb(Ti_{1-x}Zr_x)O_3$ system, *SolidState Commun*, **7**, 41-45(1969).

10 Y. Saito, H. Takano, T. Tani, T. Nonoyama, K. Takatori, T. Homma, T. Nagaya, and M. Nakamura, Lead-free piezoceramics, *Nature*, **432**, 84-87 (2004).

11 E. K. Akdogan, K. Kerman, M. Abazari, and A. Safari, Origin of high piezoelectric activity in ferroelectric $(K_{0.44}Na_{0.52}Li_{0.04})$-$(Nb_{0.84}Ta_{0.1}Sb_{0.06})O_3$ ceramics, *Appl. Phys. Lett.*, **92**, 112908 (2008).

12 E. Hollenstein, D. Damjanovic, N. Setter, Temperature stability of the piezoelectric properties of Li-modified KNN ceramics, *J. Eur. Ceram. Soc.*, **27**, 4093-4097 (2007).

13 R. Wang, K. Wang, F. Yao, J. Li, F. H. Schader, K. G. Webber, W. Jo, and J.

Rödel, Temperature Stability of Lead-Free Niobate Piezoceramics with Engineered Morphotropic Phase Boundary, *J. Am. Ceram. Soc*., **98** [7], 2177-2182 (2015).

14 H. Shi, J. Chen, R. Wang, S. Dong, Full set of material constants of $(Na_{0.5}K_{0.5})NbO_3$-$BaZrO_3$-$(Bi_{0.5}Li_{0.5})TiO_3$ lead-free piezoelectric ceramics at the morphotropic phase boundary, *J. Alloys and Compounds*, **655**, 290-295 (2016).

15 S. Zhang, A. B. Kounga, E. Aulbach, T. Granzow, W. Jo , H. Kleebe, and J. Rödel, Lead-free piezoceramics with giant strain in the system $Bi_{0.5}Na_{0.5}TiO_3$-$BaTiO_3$-$K_{0.5}Na_{0.5}NbO_3$. I. Structure and room temperature properties *J. Appl. Phys.*, **103**, 034107 (2008).

16 W. Liu and X. Ren, Large Piezoelectric Effect in Pb-Free Ceramics, *Phys. Rev. Lett.*, **103**, 257602 (2009).

17 S. Murakami, T. Watanabe, T. Suzuki, T. Matsuda, and K. Miura, Effects of poling termination and aging process on piezoelectric properties of Mn-doped $BaTi_{0.96}Zr_{0.04}O_3$ ceramics, *Jpn. J. Appl. Phys.,* **54**, 10ND05 (2015).

18 M. H. Lee, D. J. Kim, J. S. Park, S. W. Kim, T. K. Song, M. Kim, W. Kim, D. Do, and I. Jeong, High-Performance Lead-Free Piezoceramics with High Curie Temperatures, *Adv. Mater.,* **27**, 6976-6982 (2015).

19 G. Shirane, K. Suzuki, and A. Takeda, Phase Transitions in Solid Solutions of $PbZrO_3$ and $PbTiO_3$ (II) X-ray Study, *Journal of the Physical Society of Japan***, 7** (1), 12-18 (1952).

20 A. Jaffe, R. S. Roth, and S. Marzullo, Piezoelectric Properties of Lead Zirconate-Lead Titanate Solid-Solution Ceramics, *J. Appl. Phys.,* **25**, 809-810 (1954).

21 S. O. Leontsev and R. E. Eitel, Dielectric and Piezoelectric Properties in Mn-Modified (1-x)$BiFeO_3$–x$BaTiO_3$ Ceramics, *J. Am. Ceram. Soc.*, **92**, 2957-2961 (2009).

22 Y. Wei, X. Wang, J. Zhu, X. Wang, and J. Jia, Dielectric, Ferroelectric, and Piezoelectric Properties of $BiFeO_3$–$BaTiO_3$ Ceramics, *J. Am. Ceram. Soc.*, **96** [10], 3163-3168 (2013).

23 L. Cao, C. Zhou, J. Xu, Q. Li, C. Yuan, and G. Chen, Effect of poling on polarization alignment, dielectric behavior, and piezoelectricity development in polycrystalline $BiFeO_3$–$BaTiO_3$ ceramics, *Phys. Status Solidi A* **213**, No. 1, 52-59 (2016).

24 A. Singh, A. Senyshyn, H. Fuess, S.e J. Kennedy, and D. Pandey, Magnetic transitions and site-disordered induced weak ferromagnetism in (1-x)$BiFeO_3$-x$BaTiO_3$, *Phys. Rev. B,* **89**, 024108 (2014).

25 M. M. Kumar, A. Srinivas, and S. V. Suryanarayana, Structure property relations in $BiFeO_3$/$BaTiO_3$ solid solutions, *J. Appl. Phys.*, **87**, 855-862 (2000).

26 R. A. M. Gotardo, D. S. F. Viana, M. Olzon-Dionysio, S.D. Souza, D. Garcia, J. A. Eiras, M. F. S. Alves, L. F. Cótica, I. A. Santos, and A. A. Coelho, Ferroic states and phase coexistence in $BiFeO_3$-$BaTiO_3$ solid solutions, *J. Appl. Phys.*, **112**, 104112 (2012).

27 H. Yabuta, M. Shimada, T. Watanabe, J. Hayashi, M. Kubota, K. Miura, T. Fukui, and S. Wada, Microstructure of $BaTiO_3$-$Bi(Mg_{1/2}Ti_{1/2})O_3$-$BiFeO_3$ Piezoelectric Cermics, *Jpn. J. Appl. Phys*., **51**, 09LD04 (2012).

28 J. Chen, J. Chen, Enhanced thermal stability of lead-free high temperature 0.75$BiFeO_3$–0.25$BaTiO_3$ ceramics with excess Bi content, *J. Alloys and Compounds*, **589**, 115-119 (2014).

29 C. Zhou, A. Feteira, X. Shan, H. Yang, Q. Zhou, J. Cheng, W. Li, H. Wang, Remarkably high-temperature stable piezoelectric properties of $Bi(Mg_{0.5}Ti_{0.5})O_3$ modified $BiFeO_3$–$BaTiO_3$ ceramics, Appl. Phys. Lett., **101**, 032901 (2012).

30 T. Wang, L. Jin, Y. Tian, L. Shu, Q. Hu, X. Wei, Microstructure and ferroelectric properties of $Nb_2O_5$-modified $BiFeO_3$-$BaTiO_3$ lead-free ceramics for energy storage, *Materals Lett.*, **137**, 79-81 (2014).

31 Y. Jun, W. Moon, C. Chang, H. Kim, H. S. Ryu, J. W. Kim, K. H. Kim, S. Hong, Effects of Nb-doping on electric and magnetic properties in multi-ferroic $BiFeO_3$ ceramics, *Solid State Commun.*, **135**, 133-137 (2005).

32 M.S. Wu, Z.B. Huang, C.X. Han, S.L. Yuan, C.L. Lu, S.C. Xia, Enhanced multiferroic properties of $BiFeO_3$ ceramics by Ba and high-valence Nb co-doping, *Solid State Commun.*, **152**, 2142-2146 (2012).

33 Z. Yao, C. Xu, H. Hao, Q. Xu, W. Hu, M. Cao, and H. Liu, Manganese-Doped $BiFeO_3$–$BaTiO_3$ High-Temperature Piezoelectric Ceramics: Phase Structures and Defect Mechanism, Int. J. Appl. Ceram. Technol., **13** [3], 549-553 (2016).

34 Y. Guo, P. Xiao, R. Wen, Y. Wan, Q. Zheng, D. Shi, K. H. Lam, M. Liu and D. Lin, Critical roles of Mn-ions in enhancing the insulation, piezoelectricity and multiferroicity of $BiFeO_3$-based lead-free high temperature ceramics, J. Mater. Chem., **3** 5811-5824 (2015).

35 W. Zhou, Q. Zheng, Y. Li, Q. Li, Y. Wan, M. Wu, and D. Lin, Structure, ferroelectric, ferromagnetic, and piezoelectric properties of Al-modified $BiFeO_3$–$BaTiO_3$ multiferroic ceramics, *Phys. Status Solid A*, **212**, 632-639 (2015).

36 L. Luo, N. Jiang, X. Zou, D. Shi, T. Sun, Q. Zeheng, C. Xu, K. H. Lam, and D. Lin, Phase transition, piezoelectric, and multiferroic properties of $La(Co_{0.5}Mn_{0.5})O_3$-modified $BiFeO_3$–$BaTiO_3$ lead-free ceramics, *Phys. Status Solidi A*, 212, No. 9, 2012-2022 (2015).

37 Q. Zheng, , L. Luo, K. H. Lam, N. Jiang, Y. Guo, and D. Lin, Enhanced ferroelectricity, piezoelectricity, and ferromagnetism in Nd-modified $BiFeO_3$-$BaTiO_3$ lead-free ceramics, *J. Appl. Phys.*, **116**, 184101 (2014).

38 C. Zhou, Z. Cen, H. Yang, Q. Zhou, W. Li, C. Yuan, H. Wang, Structure, electrical properties of $Bi(Fe,Co)O_3$–$BaTiO_3$ piezoelectric ceramics with improved Curie temperature, *Physica B*, **410**, 13-16 (2013).

39 I. Fujii, R. Mitsui, K. Nakashima, N. Kumada, M. Shimada, T. Watanabe, J. Hayashi, H. Yabuta, M. Kubota, T. Fukui, and S. Wada, Structural, Dielectric, and Piezoelectric Properties of Mn-Doped $BaTiO_3$–$Bi(Mg_{1/2}Ti_{1/2})O_3$–$BiFeO_3$ Ceramics, *Jpn. J. Appl. Phys.*, **50**, 09ND07 (2011).

40 X. Shan, C. Zhou, Z. Cen, H. Yang, Q. Zhou, Weizhou Li, $Bi(Zn_{1/2}Ti_{1/2})O_3$

modified $BiFeO_3$–$BaTiO_3$ lead-free piezoelectric ceramics with high temperature stability, *Ceramics International*, **39**, 6707-6712 (2013).

41 L. Zhu, B. Zhang, S. Li, L. Zhao, N. Wang, X. Shi, Enhanced piezoelectric properties of $Bi(Mg_{1/2}Ti_{1/2})O_3$ modified $BiFeO_3$-$BaTiO_3$ ceramics near the morphotropic phase boundary, *J. Alloys and Compounds*, **664**, 602-608 (2016).

42 Q. Zhou, C. Zhou, H. Yang, G. Chen, W. Li, and H. Wang, Dielectric, Ferroelectric, and Piezoelectric Properties of $Bi(Ni_{1/2}Ti_{1/2})$ $O_3$-Modified $BiFeO_3$–$BaTiO_3$ Ceramics with High Curie Temperature, *J. Am. Ceram. Soc.*, **95**, 3889-3893 (2012).

43 S. Zhang, A. B. Kounga, and E. Aulbach H. Ehrenberg J. Rödel, Giant strain in lead-free piezoceramics $Bi_{0.5}Na_{0.5}TiO_3$-$BaTiO_3$-$K_{0.5}Na_{0.5}NbO_3$ system, *Appl. Phys. Lett.*, **91**, 112906 (2007).

44 E. A. Patterson, D. P. Cann, J. Pokorny, and I. M. Reaney, Electromechanical strain in $Bi(Zn_{1/2}Ti_{1/2})O_3$–$(Bi_{1/2}Na_{1/2})TiO_3$–$(Bi_{1/2}K_{1/2})TiO_3$ solid solutions, *J. Appl. Phys.*, **111**, 094105 (2012).

45 X. Liu, J. Zhai, B. Shen, F. Li, Y. Zhang, P. Li, B. Liu, Electric-field-temperature phase diagram and electromechanical properties in lead-free (Na0.5Bi0.5)TiO3-based incipient piezoelectric ceramics, *Journal of the European Ceramic Society,* **37,** 1437–1447 (2017).

46 A. Khesro, D. Wang, F. Hussain, D. C. Sinclair, A. Feteira, and I. M. Reaney, Temperature stable and fatigue resistant lead-free ceramics for actuators, *Appl. Phys. Lett.*, **109**, 142907 (2016).

47 D. Wang, A. Khesro, S. Murakami, A. Feteira, Q. Zhao, I. M. Reaney, Temperature dependent, large electromechanical strain in Nd-doped BiFeO3-BaTiO3 lead-free ceramics, *Journal of the European Ceramic Society,* **37,** 1857–1860 (2017).

48 Y. Ehara, N. Novak, A. Ayrikyan, P. T. Geiger, and K. G. Webber, Dielectric, Phase transformation induced by electric field and mechanical stress in Mn-doped

$(Bi_{1/2}Na_{1/2})TiO_3$-$(Bi_{1/2}K_{1/2})TiO_3$ ceramics, *J. Appl. Phys.*, **120**, 174103 (2016).

49 L. Li, J. Hao, R. Chu, Z. Xu, W. Li, J. Du, P. Fu, Ferroelectric and field-induced strain response of lead-free (Fe,Sb)-modified $(Bi_{0.5}Na_{0.5})_{0.935}Ba_{0.065}TiO_3$ ceramics *Ceramics International,* **42,** 9419–9425 (2016).

50 D. Wang, Y. Fotinich, G.P. Carman, Influence of temperature on the electromechanical and fatigue behavior of piezoelectric ceramics, *J. Appl. Phys.* **83**, 5342–5350 (1998).

51 W. Y. Pan, C. Q. Dam, Q. M. Zhang, and L. E. Cross, Large displacement transducers based on electric field forced phase transitions in the tetragonal (Pb0.97La0.02) (Ti,Zr,Sn)O3 family of ceramics, *J. Appl. Phys.*, **66**, 6014-6023 (1989).

52 D. Damjanovic, Ferroelectric, dielectric and piezoelectric properties of ferroelectric thin films and ceramics, *Rep. Prog. Phys.*, **61**, 1267-1324 (1998).

53 M. Davis, D. Damjanovic, and Nava Setter, Electric-field-induced orthorhombic to rhombohedral phase transition in $[111]_C$-oriented $0.92Pb.Zn_{1/3}Nb_{2/3}.O_3{-}0.08PbTiO_3$, *J. Appl. Phys.*, **97**, 064101 (2005).

54 M. Davis, D. Damjanovic, and N. Setter, Electric-field-, temperature-, and stress-induced phase transitions in relaxor ferroelectric single crystals, Phys. Rev. B, **73**, 014115 (2006).

55 A. Pramanick, D. Damjanovic, J. E. Daniels, J. C. Nino, and J. L. Jones, Origins of Electro-Mechanical Coupling in Polycrystalline Ferroelectrics During Subcoercive Electrical Loading, *J. Am. Ceram. Soc.*, **94**, [2], 293-309 (2011).

56 T. Ibn-Mohammed, SCL Koh, IM Reaney, A. Acquaye, D Wang, S Taylor, A. Genovese, Integrated hybrid life cycle assessment and supply chain environmental profile evaluations of lead-based (lead zirconate titanate) versus lead-free (potassium sodium niobate) piezoelectric ceramics, Energy & Env. Sci.

9 (11), 3495-3520 (2016).

Table 1. Lattice parameters (a, b, c), fraction of phase (*wt%*) and fitting parameters ($R_{wp}$ and $\chi^2$) for $0.05Bi(Mg_{2/3}Nb_{1/3})O_3$-(0.95-x)$BaTiO_3$-x$BiFeO_3$ (x = 0.55, 0.60, 0.63, 0.65, 0.70, and 0.75) ceramics measured at room temperature.

| x | Space group | Lattice parameters | | | Weight (%) | R-factors | | |
|---|---|---|---|---|---|---|---|---|
| | | a (Å) | b (Å) | c (Å) | | $R_{wp}$ (%) | $R_p$ (%) | $\chi^2$ |
| 0.55 | Pm-3m | 4.0007(9) | 4.0007(9) | 4.0007(9) | | 9.41 | 7.37 | 2.78 |
| 0.60 | Pm-3m | 3.9988(1) | 3.9988(1) | 3.9988(1) | | 9.51 | 7.46 | 3.07 |
| 0.63 | Pm-3m | 3.9980(8) | 3.9980(8) | 3.9980(8) | 85.3 | 9.70 | 7.69 | 1.36 |
| | R3c | 5.6145(0) | 5.6145(0) | 14.0691(7) | 14.7 | | | |
| 0.65 | Pm-3m | 3.9967(6) | 3.9967(6) | 3.9967(6) | 86.5 | 10.3 | 8.29 | 1.67 |
| | R3c | 5.6573(8) | 5.6573(8) | 13.7388(5) | 13.5 | | | |
| 0.70 | Pm-3m | 3.9994(6) | 3.9994(6) | 3.9994(6) | 31.6 | 9.64 | 7.40 | 3.39 |
| | R3c | 5.6352(6) | 5.6352(6) | 13.8498(9) | 68.4 | | | |
| 0.75 | Pm-3m | 3.9982(3) | 3.9982(3) | 3.9982(3) | 13.3 | 9.40 | 7.33 | 3.04 |
| | R3c | 5.6272(6) | 5.6272(6) | 13.8844(2) | 86.7 | | | |

Table 2. Capacitance measured at 320°C (from *Z"* peak) and activation energy for the dc conductivity for $0.05Bi(Mg_{2/3}Nb_{1/3})O_3$-(0.95-x)$BaTiO_3$-x$BiFeO_3$ (x = 0.55, 0.60, 0.63, 0.65, 0.70, and 0.75) ceramics.

| x | Capacitance at 320°C C (nF/cm) | Activation Energy $E_a$ (eV) |
|---|---|---|
| 0.55 | 1.01 | 1.12 |
| 0.60 | 1.98 | 1.11 |
| 0.63 | 1.59 | 1.15 |
| 0.65 | 1.17 | 1.14 |
| 0.70 | 0.43 | 1.11 |
| 0.75 | 0.13 | 0.87 |

Table 3. Comparison of the temperature dependence of strain (*ΔS*) for several kinds of piezoelectric ceramics (PZT, $Bi_{1/2}K_{1/2}TiO_3$-BF, $Bi_{1/2}Na_{1/2}TiO_3$- $Bi_{1/2}K_{1/2}TiO_3$, BT-BF,

BMN-BT-BF).

| Material | Temperature Range | $\Delta S$ | Reference |
|---|---|---|---|
| PZT 4 | RT-160°C | 15% | 10 |
| PZT-5H | RT-80°C | >40% | 50 |
| 0.91BKT-0.09BF | RT-175°C | 15% | 46 |
| BNT-BKT | RT-190°C | 3% | 48 |
| 0.3BT-0.7BF | RT-150°C | 42% | 47 |
| 0.05BMN-0.32BT-0.63BF | RT-175°C | 25% | This work |

**FIGURE 1** XRD patterns of $0.05Bi(Mg_{2/3}Nb_{1/3})O_3$-$(0.95-x)BaTiO_3$-$xBiFeO_3$ (x = 0.55, 0.60, 0.63, 0.65, 0.70, and 0.75) ceramics measured at room temperature. Indexation for x = 0.55 and 0.75 are in pseudocubic and rhombohedral settings, respectively.

**FIGURE 2** BSE images of polished surface of $0.05Bi(Mg_{2/3}Nb_{1/3})O_3$-$(0.95-x)BaTiO_3$-$xBiFeO_3$ ceramics with $x$ = (a) 0.55, (b) 0.60, (c) 0.63, (d) 0.65, (e) 0.70 and (f) 0.75. Residual flaws and irregularities are caused by polishing and thermal etching.

**FIGURE 3** a) Two beam dark field transmission electron microscopy image of a sample with $\underline{x}$ = 0.63 obtained using a 111 reflection close to the [110] direction, illustrating the nanodomain structure of the pseudocubic relaxor-like phase. Inset is the [110] zone axis diffraction pattern in which only fundamental perovskite reflections are apparent. b) Bright field image of $x$ = 0.7 close to the [112] direction. Bottom LHS shows lamellar ferroelectric domains and the top RHS exhibits a similar domain structure on tilting. Inset are two variants of the [112] zone axis for the R3c phase with and without ½{ooo} antiphase tilt reflections.

**FIGURE 4** Combined $Z''$ and $M''$ spectroscopic plots for $0.05Bi(Mg_{2/3}Nb_{1/3})O_3$-$(0.95-x)BaTiO_3$-$(x)BiFeO_3$ ceramics with $x$ = (a) 0.55, (b) 0.60, (c) 0.63, (d) 0.65, (e) 0.70 measured at 320°C and (f) x = 0.75 measured at 180°C.

**FIGURE 5** Arrhenius plot of the *dc* electrical conductivity for $0.05Bi(Mg_{2/3}Nb_{1/3})O_3$-$(0.95-x)BaTiO_3$-$xBiFeO_3$ (x = 0.55, 0.60, 0.63, 0.65, 0.70, and 0.75) ceramics.

**FIGURE 6** Temperature dependence of (a) $\varepsilon_r$ and (b) $\tan\delta$ for $0.05Bi(Mg_{2/3}Nb_{1/3})O_3$-$(0.95-x)BaTiO_3$-$xBiFeO_3$ (x = 0.55, 0.60, 0.63, 0.65, 0.70, and 0.75) ceramics.

**FIGURE 7** Frequency dependence of relative permittivity and dielectric loss, tanδ vs temperature for 0.05 $(Mg_{2/3}Nb_{1/3})O_3$-(1-x)$BaTiO_3$-x$BiFeO_3$ ceramics (*x* = (a) 0.55, (b) 0.63, (c) 0.70.

**FIGURE 8** (a) *PE* hysteresis loops and (b) bipolar *SE* curves for 0.05Bi$(Mg_{2/3}Nb_{1/3})O_3$-(0.95-x)$BaTiO_3$-x$BiFeO_3$ (x = 0.55, 0.60, 0.63, 0.65, 0.70, and 0.75) ceramics measured at room temperature.

**FIGURE 9** Unipolar *SE* curve of (a) unpoled and (b) poled and unpoled samples of 0.05Bi$(Mg_{2/3}Nb_{1/3})O_3$-(0.95-x)$BaTiO_3$-x$BiFeO_3$ (x = 0.63) ceramics measured at room temperature.

**FIGURE 10** The temperature dependence of the unipolar *SE* curve for poled 0.05Bi$(Mg_{2/3}Nb_{1/3})O_3$-(0.95-x)$BaTiO_3$-x$BiFeO_3$ (x = 0.63) ceramics measured under an electric field of 6 kV/mm from 25 to 175 ºC.

**FIGURE 11** The largest $d_{33}^*$ calculated from unipolar strain and $d_{33}$ for 0.05Bi$(Mg_{2/3}Nb_{1/3})O_3$-(0.95-x)$BaTiO_3$-(x)$BiFeO_3$ (x = 0.55, 0.60, 0.63, 0.65, 0.70, and 0.75) ceramics measured at room temperature.

**FIGURE 12** BSE images of polished surface of (a) furnace cooled and (b) quenched 0.05Bi$(Mg_{2/3}Nb_{1/3})O_3$-(0.95-x)$BaTiO_3$-(x)$BiFeO_3$ (x = 0.75) ceramics.

**FIGURE 13** (a) *PE* hysteresis loops and (b) bipolar *SE* curves for furnace cooled and quenched 0.05Bi$(Mg_{2/3}Nb_{1/3})O_3$-(0.95-x)$BaTiO_3$-x$BiFeO_3$ (x = 0.75) ceramics measured at room temperature.

**FIGURE 14** (a) Cross-sectional SEM image, (b) *PE* hysteresis loop and *SE* curve measured at room temperature, and temperature dependence of (c) unipolar strain and (d) *PE* loop of MLA for 0.05Bi$(Mg_{2/3}Nb_{1/3})O_3$-(0.95-x)$BaTiO_3$-x$BiFeO_3$ (x = 0.63).

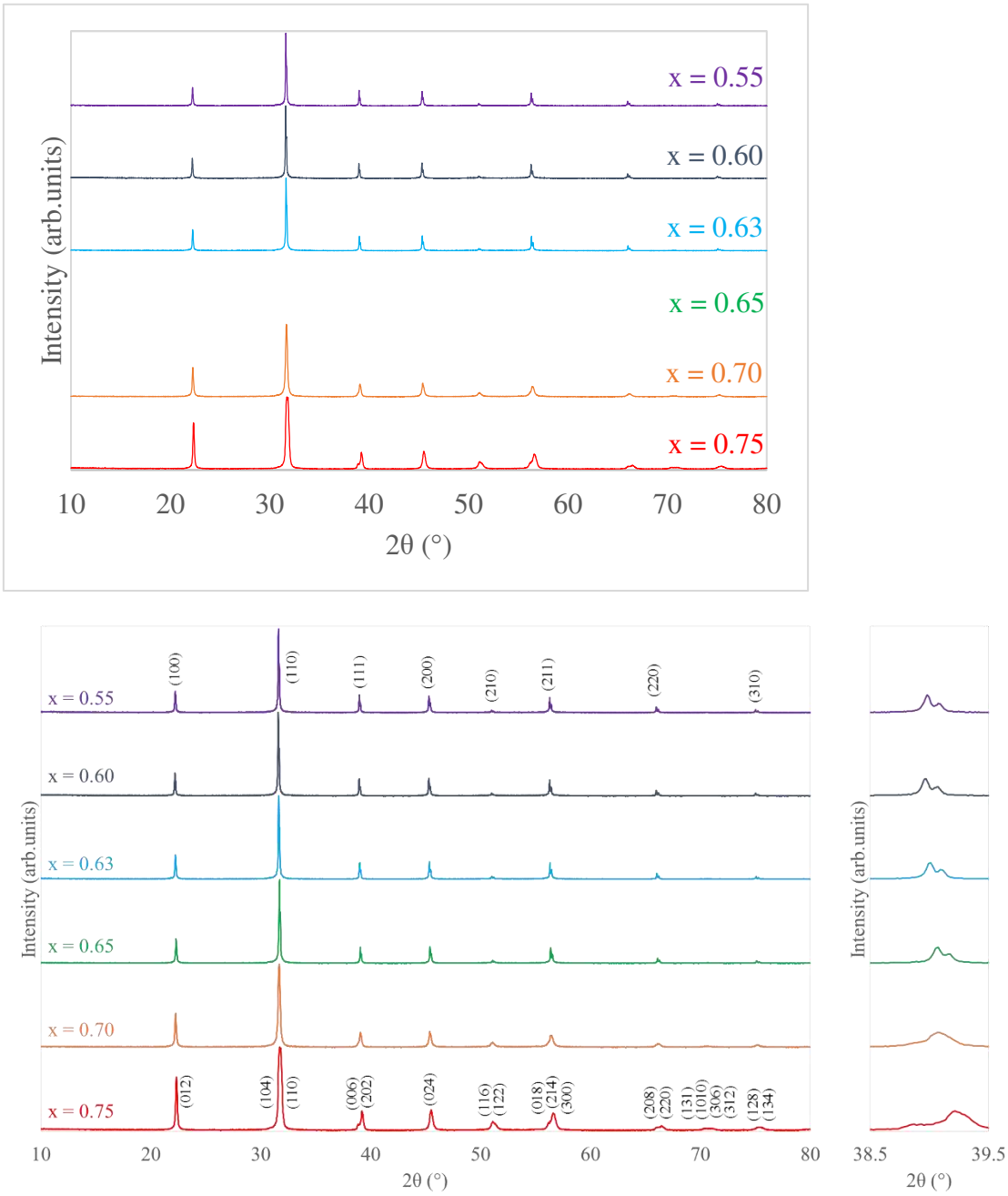


Fig. 1. XRD patterns of $0.05Bi(Mg_{2/3}Nb_{1/3})O_3$-(0.95-x)$BaTiO_3$-x$BiFeO_3$ (x = 0.55, 0.60, 0.63, 0.65, 0.70, and 0.75) ceramics measured at room temperature.

Table 1. Lattice parameters (*a*, *b* and *c*), fraction of phase (wt%) and fitting parameters ($R_{wp}$ and $\chi^2$) for $0.05Bi(Mg_{2/3}Nb_{1/3})O_3$-(0.95-x)$BaTiO_3$-(x)$BiFeO_3$ (x = 0.55, 0.60, 0.63, 0.65, 0.70, and 0.75) ceramics measured at room temperature.

| x | Space group | Lattice parameters | | | Weight (%) | R-factors | | |
|---|---|---|---|---|---|---|---|---|
| | | a(Å) | b(Å) | c(Å) | | $R_{wp}$ (%) | $R_p$ (%) | $\chi^2$ |
| 0.55 | Pm-3m | 4.0007(9) | 4.0007(9) | 4.0007(9) | | 9.41 | 7.37 | 2.78 |
| 0.60 | Pm-3m | 3.9988(1) | 3.9988(1) | 3.9988(1) | | 9.51 | 7.46 | 3.07 |
| 0.63 | Pm-3m | 3.9980(8) | 3.9980(8) | 3.9980(8) | 85.3 | 9.70 | 7.69 | 1.36 |
| | R3c | 5.6145(0) | 5.6145(0) | 14.0691(7) | 14.7 | | | |
| 0.65 | Pm-3m | 3.9967(6) | 3.9967(6) | 3.9967(6) | 86.5 | 10.3 | 8.29 | 1.67 |
| | R3c | 5.6573(8) | 5.6573(8) | 13.7388(5) | 13.5 | | | |
| 0.70 | Pm-3m | 3.9994(6) | 3.9994(6) | 3.9994(6) | 31.6 | 9.64 | 7.40 | 3.39 |
| | R3c | 5.6352(6) | 5.6352(6) | 13.8498(9) | 68.4 | | | |
| 0.75 | Pm-3m | 3.9982(3) | 3.9982(3) | 3.9982(3) | 13.3 | 9.40 | 7.33 | 3.04 |
| | R3c | 5.6272(6) | 5.6272(6) | 13.8844(2) | 86.7 | | | |

(a)

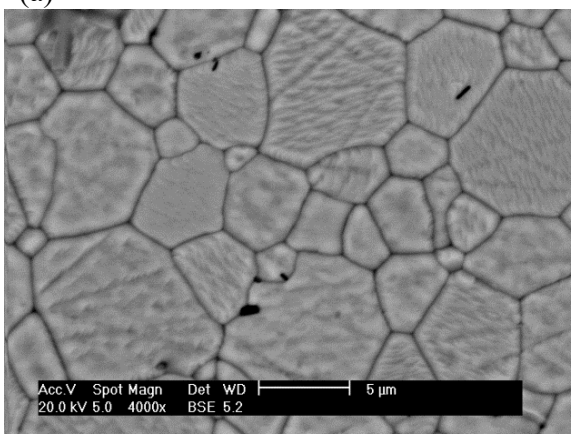


(b)

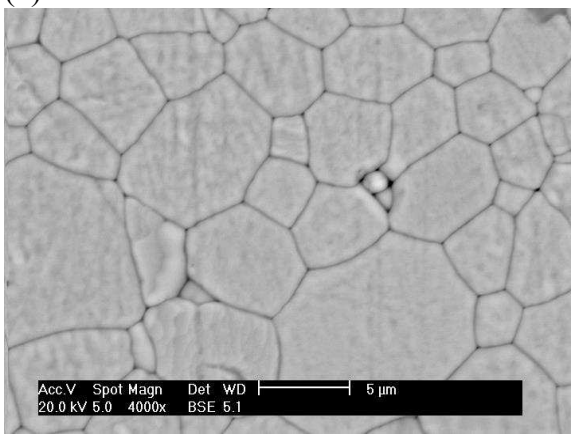


(c)

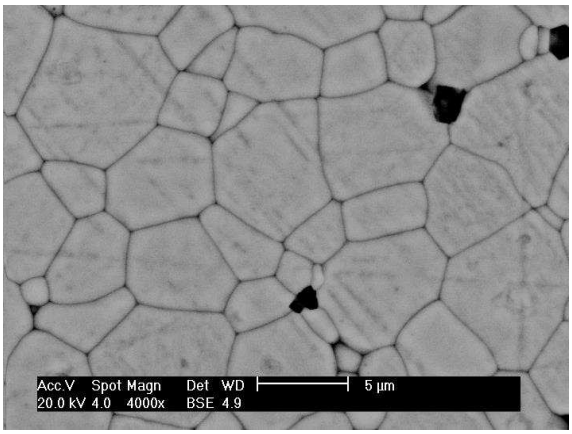


(d)

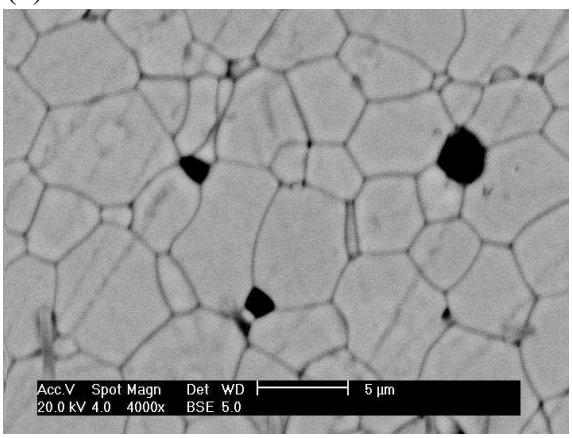


(e)

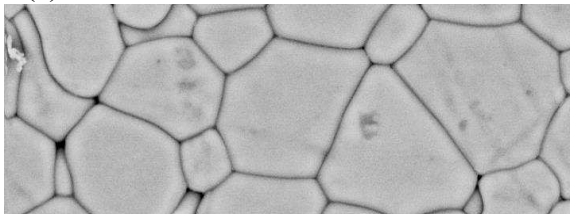

(f)

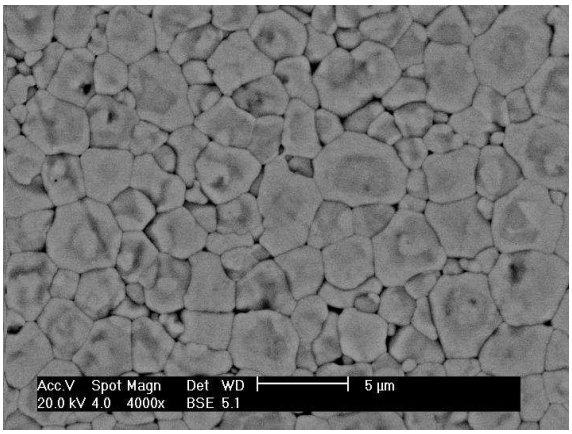


Fig. 2. BSE images of polished surface of $0.05Bi(Mg_{2/3}Nb_{1/3})O_3$-$(0.95-x)BaTiO_3$-$xBiFeO_3$ ceramics for $x$ = (a) 0.55, (b) 0.60, (c) 0.63, (d) 0.65, (e) 0.70 and (f) 0.75. Residual flaws and irregularities are caused by polishing and thermal etching.

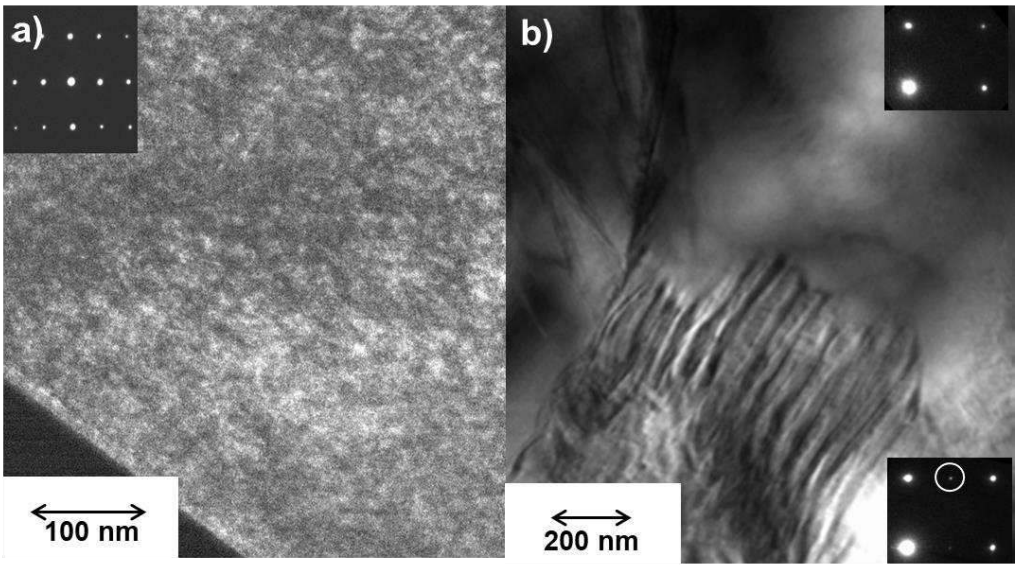


Fig. 3. a) Two beam dark field transmission electron microscopy image of a sample with $\underline{x}$ = 0.63 obtained using a 111 reflection close to the [110] direction, illustrating the nanodomain structure of the pseudocubic relaxor-like phase. Inset is the [110] zone axis diffraction pattern in which only fundamental perovskite reflections are apparent. b) Bright field image of $x$ = 0.7 close to the [112] direction. Bottom LHS shows lamellar ferroelectric domains and the top RHS exhibits a similar domain structure on tilting. Inset are two variants of the [112] zone axis for the R3c phase with and without ½{ooo} antiphase tilt reflections

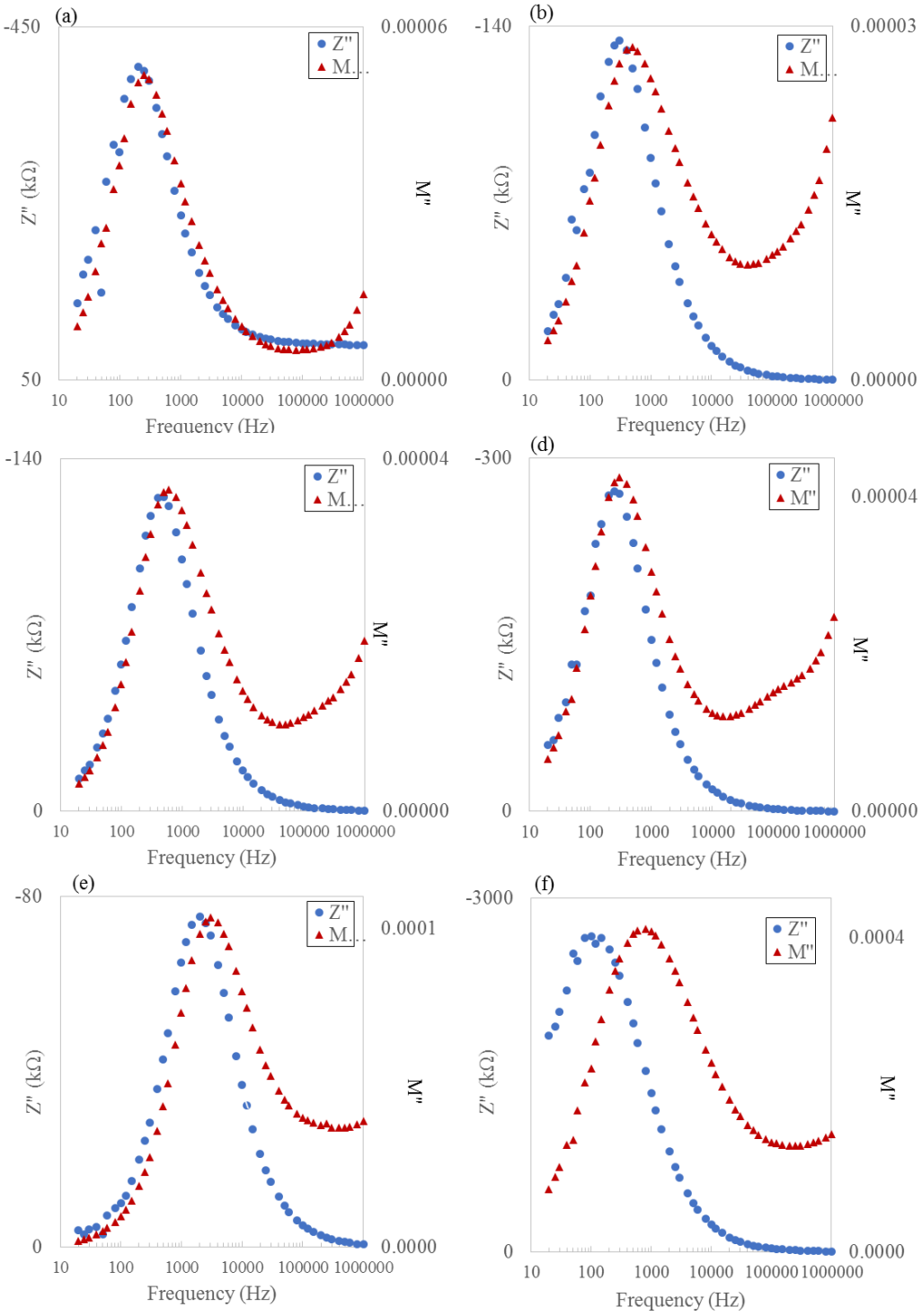


Fig. 4. Combined *Z"* and *M"* spectroscopic plots for $0.05Bi(Mg_{2/3}Nb_{1/3})O_3$-(0.95-x)$BaTiO_3$-x$BiFeO_3$ ceramic with x = (a) 0.55, (b) 0.60, (c) 0.63, (d) 0.65, (e) 0.70 measured at 320°C and (f) 0.75 and measured at 180°C.

Table 2. Capacitance measured at 320°C (from *Z"* peak) and activation energy for the *dc* conductivity for $0.05Bi(Mg_{2/3}Nb_{1/3})O_3$-(0.95-x)$BaTiO_3$-x$BiFeO_3$ (x = 0.55, 0.60, 0.63, 0.65, 0.70, and 0.75) ceramics.

| x | Capacitance at 320°C C (nF/cm) | Activation Energy $E_a$ (eV) |
|---|---|---|
| 0.55 | 1.01 | 1.12 |
| 0.60 | 1.98 | 1.11 |
| 0.63 | 1.59 | 1.15 |
| 0.65 | 1.17 | 1.14 |
| 0.70 | 0.43 | 1.11 |
| 0.75 | 0.13 | 0.87 |

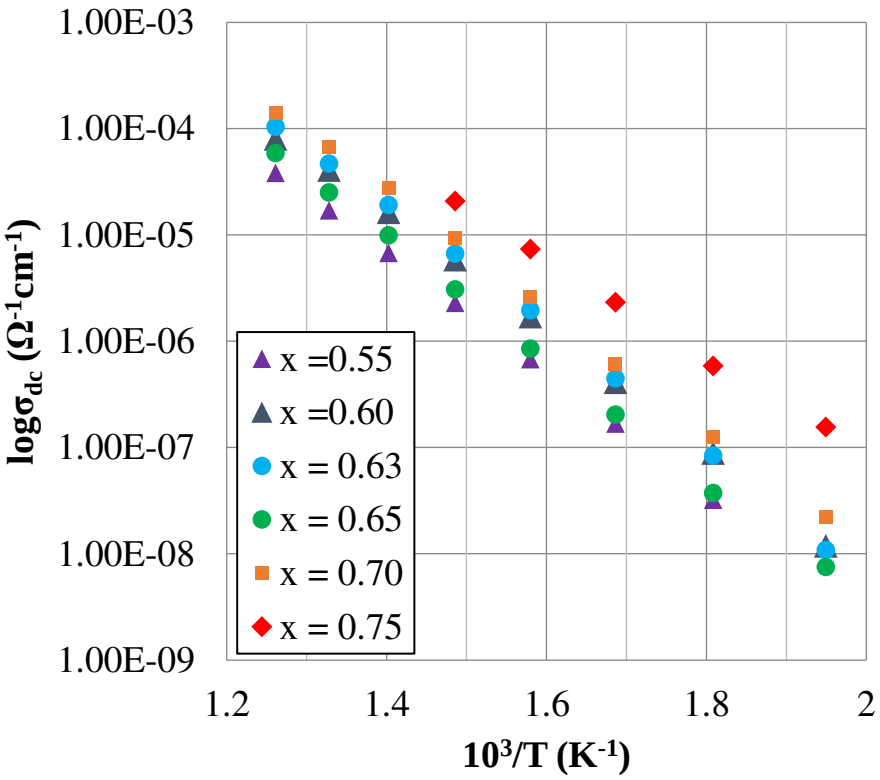


Fig. 5. Arrhenius plot of the dc electrical conductivity for $0.05Bi(Mg_{2/3}Nb_{1/3})O_3$-(0.95-x)$BaTiO_3$-x$BiFeO_3$ (x = 0.55, 0.60, 0.63, 0.65, 0.70, and 0.75) ceramics.

(a)

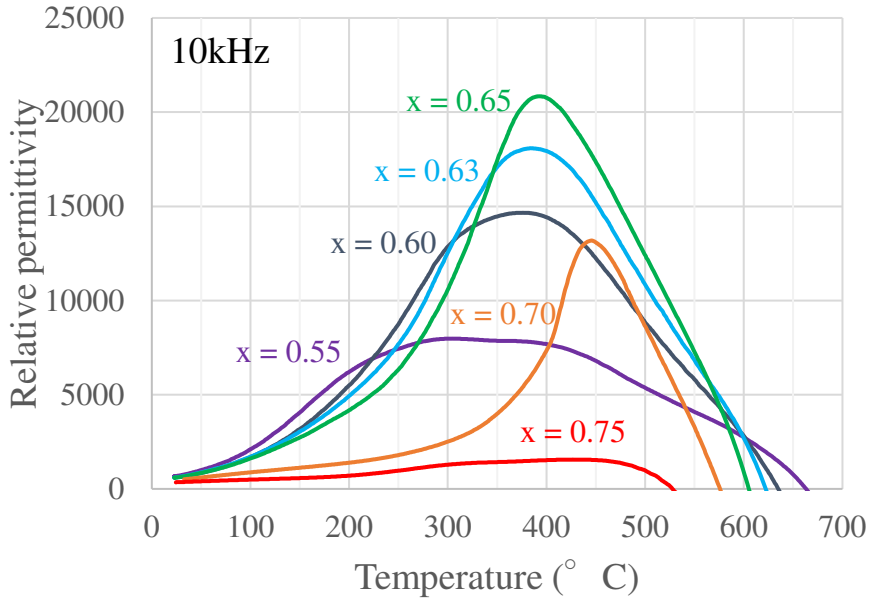


(b)

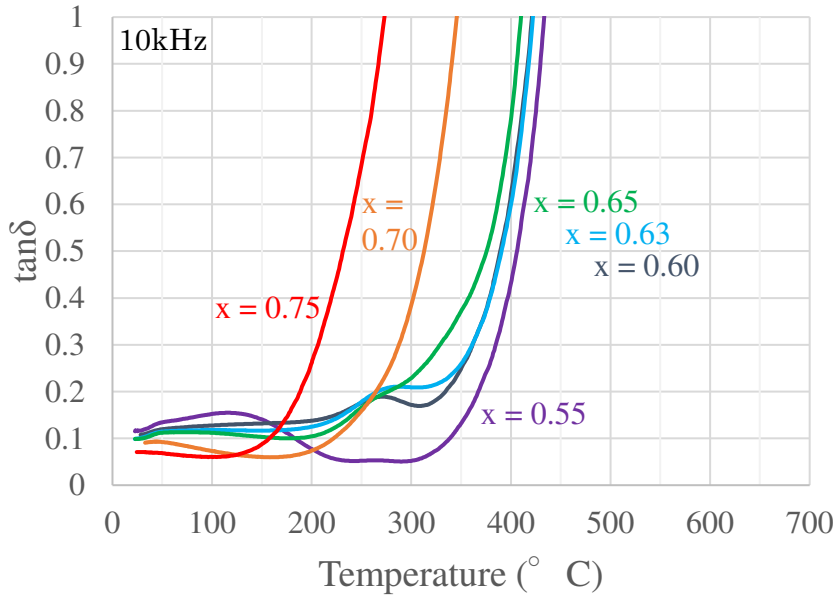


Fig. 6. Temperature dependence of (a) relative permittivity and (b) dielectric loss, tanδ for $0.05Bi(Mg_{2/3}Nb_{1/3})O_3$-(0.95-x)$BaTiO_3$-(x)$BiFeO_3$ (x = 0.55, 0.60, 0.63, 0.65, 0.70, and 0.75) ceramics.

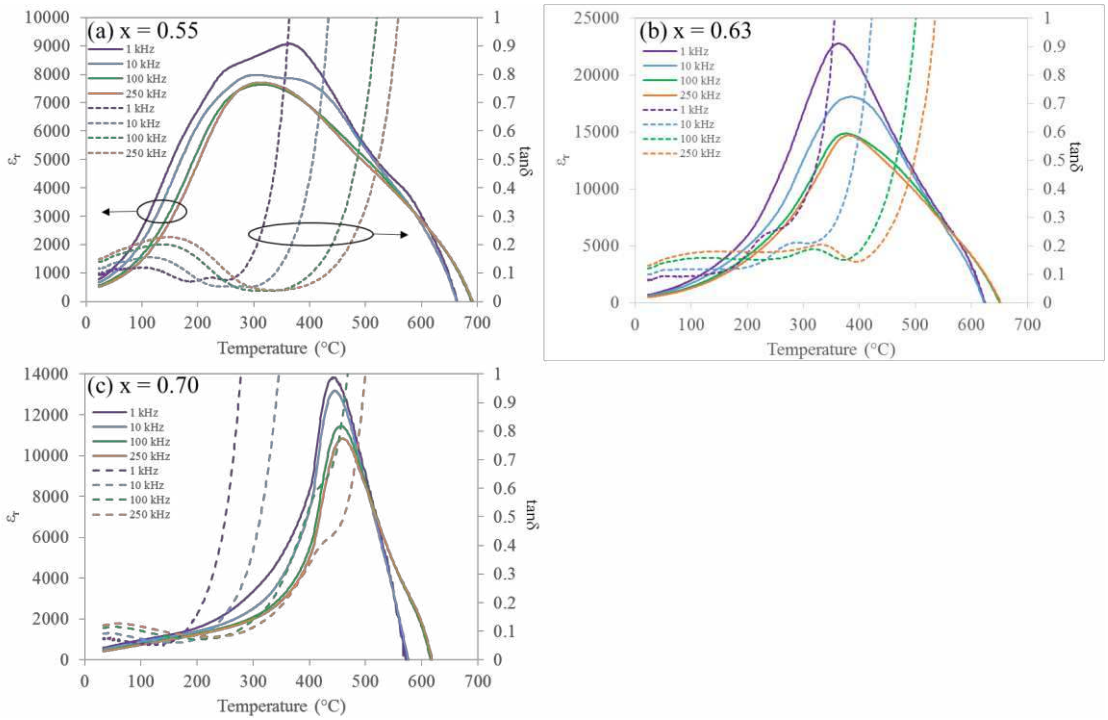


Fig. 7. Frequency dependence of relative permittivity and tanδ vs temperature for $0.05Bi(Mg_{2/3}Nb_{1/3})O_3$-(0.95-x)$BaTiO_3$-(x)$BiFeO_3$ (x = (a) 0.55, (b) 0.63, and (c) 0.70).

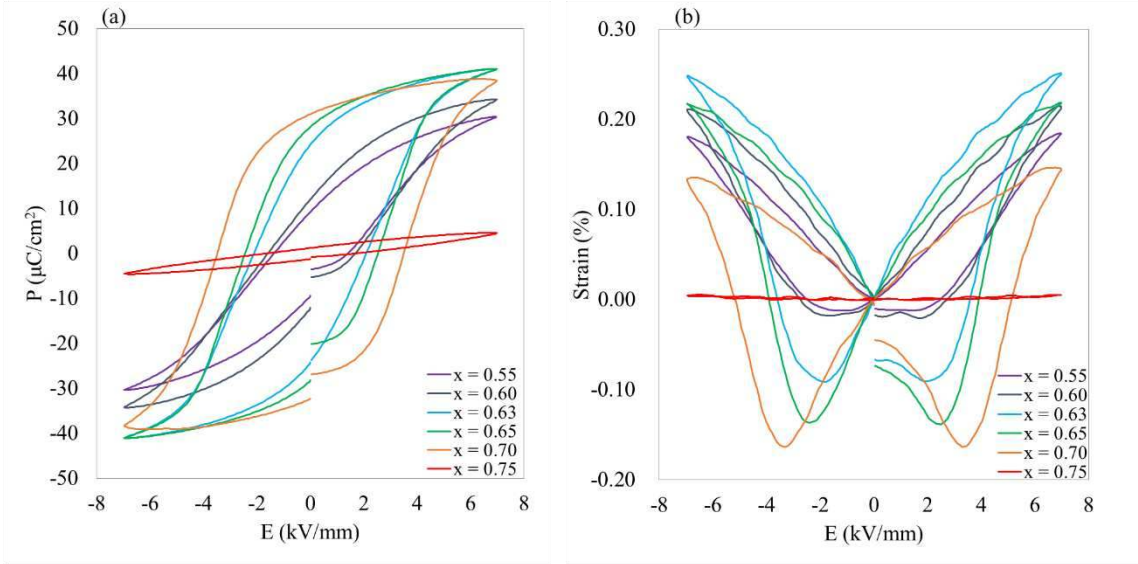


Fig. 8. (a) PE hysteresis loops and (b) bipolar *SE* curves for $0.05Bi(Mg_{2/3}Nb_{1/3})O_3$-(0.95-x)$BaTiO_3$-x$BiFeO_3$ (x = 0.55, 0.60, 0.63, 0.65, 0.70, and 0.75) ceramics measured at room temperature.

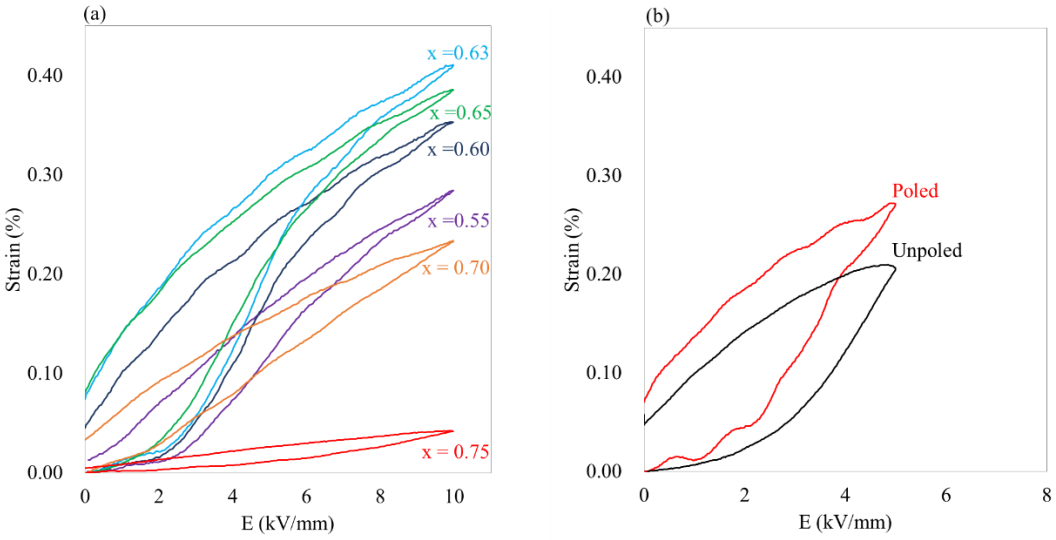


Fig. 9. Unipolar *SE* curve of (a) unpoled and (b) poled and unpoled samples of $0.05Bi(Mg_{2/3}Nb_{1/3})O_3$-$(0.95-x)BaTiO_3$-$xBiFeO_3$ (x = 0.63) ceramics measured at room temperature.

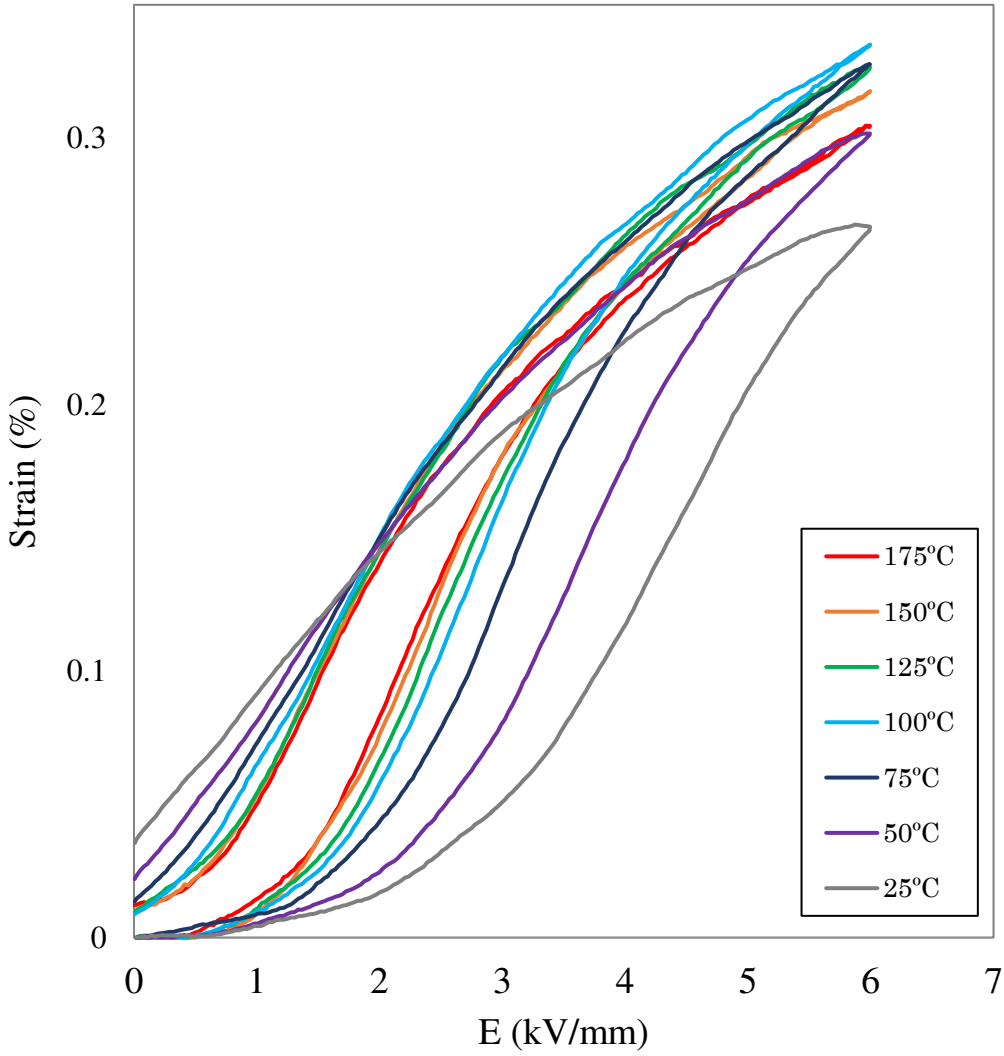


Fig. 10. The temperature dependence of the unipolar SE curve for poled $0.05Bi(Mg_{2/3}Nb_{1/3})O_3$-$(0.95-x)BaTiO_3$-$xBiFeO_3$ (x = 0.63) ceramics measured under an electric field of 6 kV/mm from 25 to 175 ºC.

Table 3. Comparison of the temperature dependence of strain (ΔS) for several kinds of piezoelectric ceramics (PZT, $Bi_{1/2}K_{1/2}TiO_3$-BF, $Bi_{1/2}Na_{1/2}TiO_3$- $Bi_{1/2}K_{1/2}TiO_3$, BT-BF, BMN-BT-BF).

| Material | Temperature Range | ΔS | Reference |
|---|---|---|---|
| PZT 4 | RT-160°C | 15% | 10 |
| PZT-5H | RT-80°C | >40% | 47 |
| 0.91BKT-0.09BF | RT-175°C | 15% | 43 |
| BNT-BKT | RT-190°C | 3% | 45 |
| 0.3BT-0.7BF | RT-150°C | 42% | 44 |
| 0.05BMN-0.32BT-0.63BF | RT-175°C | 25% | This work |

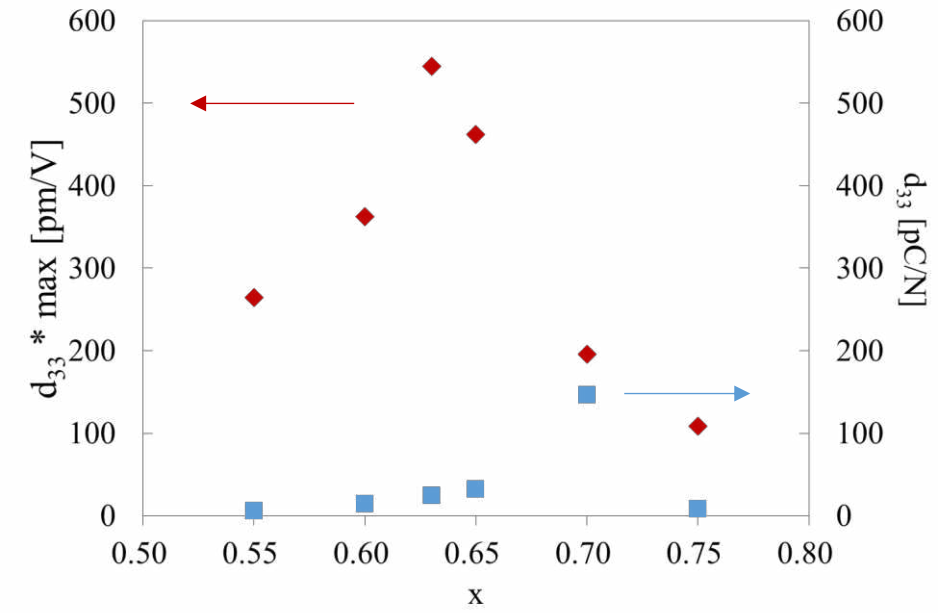


Fig. 11. The largest $d_{33}^*$ calculated from unipolar strain and $d_{33}$ for $0.05Bi(Mg_{2/3}Nb_{1/3})O_3$-$(0.95-x)BaTiO_3$-$xBiFeO_3$ (x = 0.55, 0.60, 0.63, 0.65, 0.70, and 0.75) ceramics measured at room temperature.

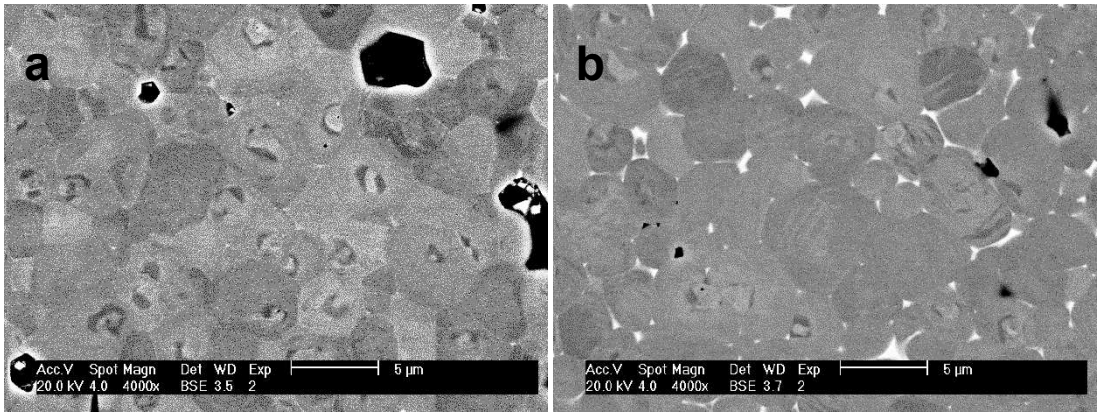


Fig. 12. BSE images of polished surface of (a) furnace cooled and (b) quenched $0.05Bi(Mg_{2/3}Nb_{1/3})O_3$-$(0.95-x)BaTiO_3$-$xBiFeO_3$ (x = 0.75) ceramics.

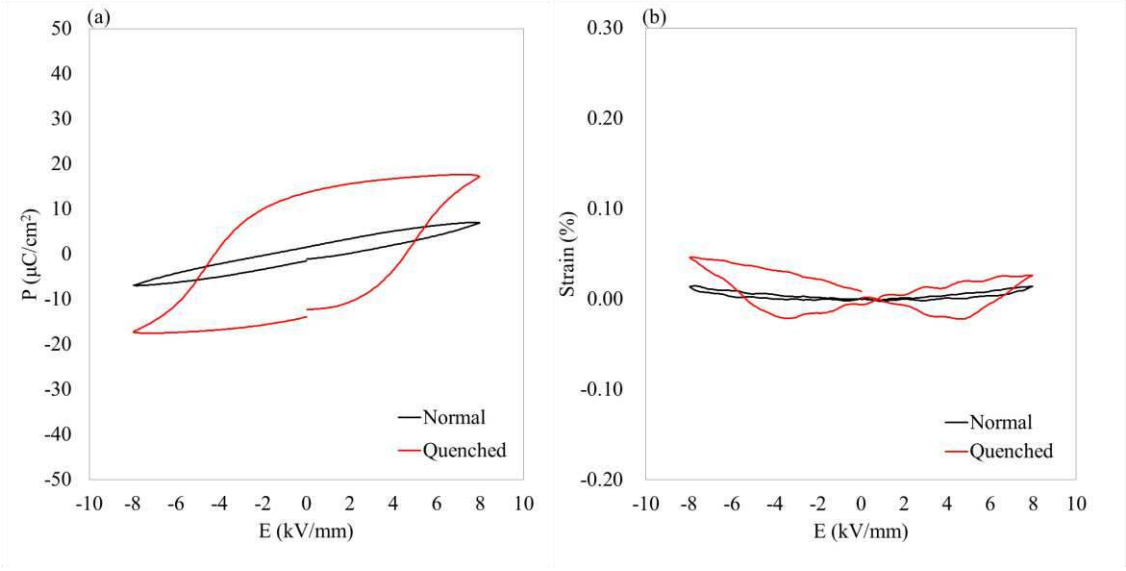


Fig. 13. (a) *PE* hysteresis loops and (b) bipolar **SE** curves for furnace cooled and quenched $0.05Bi(Mg_{2/3}Nb_{1/3})O_3$-$(0.95-x)BaTiO_3$-$xBiFeO_3$ (x = 0.75) ceramics measured at room temperature.

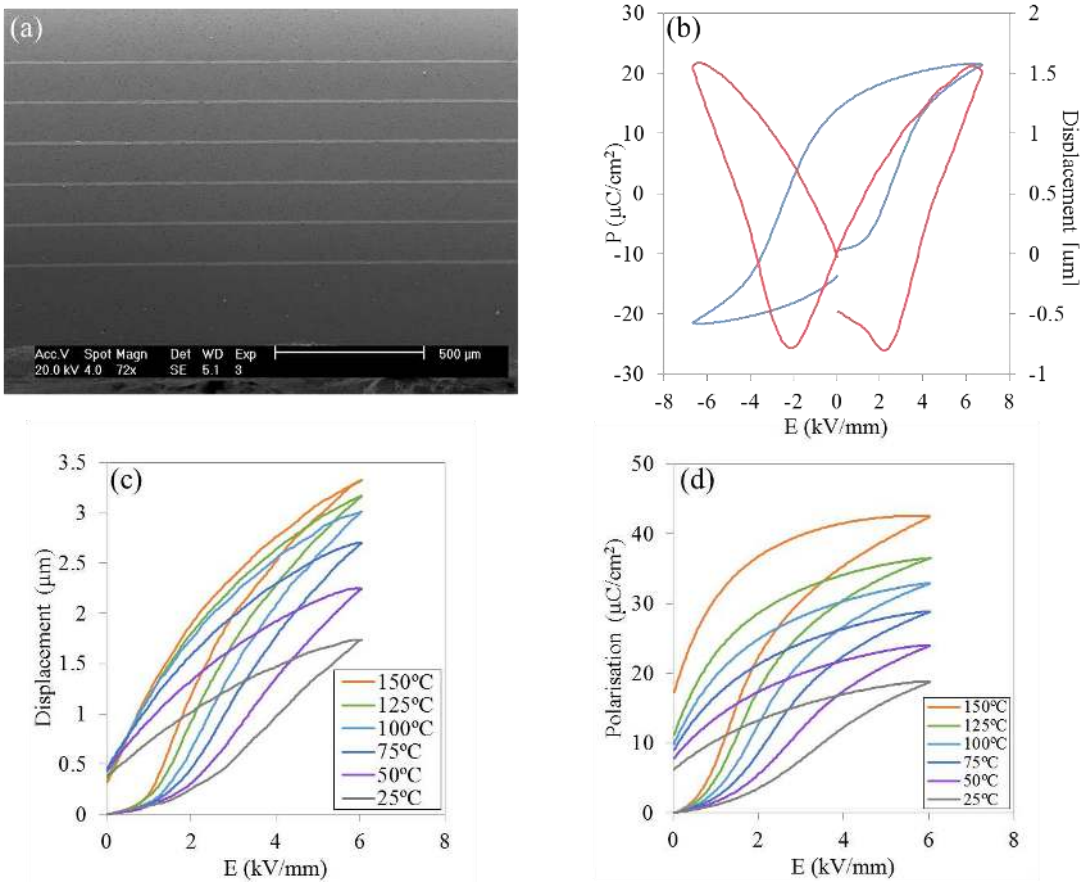


Fig. 14 (a) Cross-section SEM image, (b) PE hysteresis loop and SE curve measured at room temperature, and temperature dependence of (c) unipolar strain and (d) polarisation a multilayer actuator fabricated from $0.05Bi(Mg_{2/3}Nb_{1/3})O_3$-$(0.95-x)BaTiO_3$-$xBiFeO_3$ (x = 0.63).